











Cite this: *Nanoscale*, 2025, **17**, 19182

## Insights into the formation of free radicals using metal ferrite nanocatalysts (MFe<sub>2</sub>O<sub>4</sub>, M = Fe, Mn, Zn, Co) prepared by a highly reproducible microwave-assisted polyol method†

Alvaro Gallo-Cordova, \*‡<sup>a</sup> Nahuel Nuñez, ‡<sup>b,c,d</sup> Carlos Díaz-Ufano,<sup>a</sup> Sabino Veintemillas-Verdaguer, <sup>a</sup> Jimena Soler-Morala, <sup>a</sup> F. Javier Palomares, <sup>a</sup> Enio Lima, Jr., <sup>b,c</sup> Elin L. Winkler \*<sup>b,c</sup> and María del Puerto Morales \*<sup>a</sup>

Metal ferrite nanocatalysts possess renowned catalytic properties in advanced oxidation processes. This study aims to elucidate the impact of various parameters on their catalytic activity by measuring the formation of reactive oxygen species. Utilizing a microwave-assisted polyol method, we designed specific catalysts, demonstrating high reproducibility (>95%) of their structural, colloidal, and magnetic properties. Electron paramagnetic resonance (EPR) analysis described intricate catalytic dynamics influenced by buffer composition, particle size, and transition metal doping. The presence of buffer in the EPR measurement of the maghemite nanocatalyst with a size of 14 ± 3 nm induced a secondary reaction between <sup>•</sup>OOH and the DMPO spin-trap, shielding the radical signal by primarily generating CH<sub>3</sub> radicals, potentially hindering degradation. Smaller maghemite nanocatalysts (8 ± 2 nm) exhibited enhanced radical production due to increased surface area. Upon metal doping, manganese enhances <sup>•</sup>OOH radical production, while zinc inhibits ROS formation, and cobalt exerts nuanced influence. Additionally, catalytic efficiency in methylene blue degradation varied with the radical species, highlighting <sup>•</sup>OH radicals' superiority for rapid degradation (1 h) over <sup>•</sup>OOH (24 h). Overall, this research provides valuable insights into nanoparticle synthesis, radical formation kinetics, and catalytic performance, contributing to the advancement of sustainable catalysis for environmental remediation.

Received 19th May 2025,  
Accepted 18th July 2025  
DOI: 10.1039/d5nr02101d  
rsc.li/nanoscale

## 1. Introduction

Nanotechnology has significantly advanced our understanding and manipulation of materials at the molecular level, leading to the development of novel compounds with unique properties. Among these, metal ferrite nanoparticles have garnered considerable attention due to their potential applications in environmental catalysis.<sup>1–3</sup> Their activity, primarily catalyzed by hetero-

geneous Fenton-based reactions, involves the decomposition of hydrogen peroxide (H<sub>2</sub>O<sub>2</sub>) into reactive oxygen species (ROS) such as hydroxyl radicals (<sup>•</sup>OH) and hydroperoxyl radicals (<sup>•</sup>OOH).<sup>4–6</sup> Therefore, the catalytic activity of ferrite nanoparticles is directly related to the type and amount of ROS they are able to produce, as they are the ones responsible for degrading organic matter into carbon dioxide, water and inorganic byproducts.

Electron paramagnetic resonance (EPR) stands out as a highly sensitive technique for identifying and quantifying individual ROS. In fact, by considering EPR measurements, it has been possible to identify that the formation of specific radicals is directly linked with the surface composition of the nanoparticles (e.g. <sup>•</sup>OH radicals produced by Fe<sup>2+</sup> and <sup>•</sup>OOH by Fe<sup>3+</sup>).<sup>7,8</sup> In recent years, the incorporation of transition metals into the spinel structure of iron oxide nanoparticles has emerged as a significant factor influencing their reactivity toward H<sub>2</sub>O<sub>2</sub>.<sup>9,10</sup> Studies, such as the work by Moreno *et al.*, have demonstrated that ferrite nanoparticles upon substitution with other transition metals like nickel or manganese exhibit a notable difference in the generation of <sup>•</sup>OH and <sup>•</sup>OOH radicals in comparison with Fe ferrites, including an enhanced activity

<sup>a</sup>Departamento de Nanociencia y Nanotecnología, Instituto de Ciencia de Materiales de Madrid, ICMM/CSIC, C/Sor Juana Inés de la Cruz 3, 28049 Madrid, Spain.

E-mail: alvaro.gallo@csic.es, puerto@icmm.csic.es

<sup>b</sup>Departamento Magnetismo y Materiales Magnéticos, Gerencia de Física, Centro Atómico Bariloche, Av. Bustillo 9500, (8400) S. C. de Bariloche (RN), Argentina.  
E-mail: winkler@cab.cnea.gov.ar

<sup>c</sup>Instituto de Nanociencia y Nanotecnología, CNEA/CONICET, Nodo Bariloche, Av. Bustillo 9500, (8400) S. C. de Bariloche (RN), Argentina

<sup>d</sup>Escuela de Doctorado UAM, Centro de Estudios de Posgrado, Universidad Autónoma de Madrid, C/Francisco Tomás y Valiente, 2, 28049 Madrid, Spain

† Electronic supplementary information (ESI) available. See DOI: <https://doi.org/10.1039/d5nr02101d>

‡ These authors contributed equally.



for some materials, as measured by EPR.<sup>11</sup> Similar to iron, other divalent cations like copper have distinct pathways in AOPs, wherein they can alternate between their oxidized ( $\text{Cu}^{2+}$ ) and reduced ( $\text{Cu}^+$ ) states.<sup>12,13</sup> This redox cycling ability enables copper to participate in Fenton-like reactions, catalyzing the decomposition of  $\text{H}_2\text{O}_2$  to produce  $\cdot\text{OH}$  radicals.

Although recent studies, like the above-mentioned work, have shed light on the role of transition metals in influencing the formation of ROS in metal ferrite nanoparticles, there remains significant work to be carried out to fully comprehend these mechanisms.<sup>14</sup> Specifically, understanding how different transition metals alter the catalytic pathways leading to ROS production is essential for harnessing the full potential of metal ferrite nanocatalysts in environmental applications. Although theoretical simulations like density functional theory (DFT) have proved useful in providing insights into the electronic structure and dopant effects, their application in these systems is limited by the complexity of modeling structural disorder, surface states, and dynamic behavior. In particular, introducing a dopant into the magnetite lattice leads to a complex rearrangement of local atomic and electronic environments that is challenging to capture accurately within standard DFT frameworks.<sup>15</sup> As such, experimental validation is essential to support and refine theoretical models. Future research efforts should focus on elucidating the underlying chemical processes and kinetics governing ROS generation, considering factors such as dopant concentration, nanoparticle morphology, and reaction conditions.

In previous studies, we examined the efficacy of iron oxide nanocatalysts in the degradation of model compounds,<sup>16,17</sup> real wastewater samples,<sup>18</sup> and emergent contaminants<sup>19</sup> using magnetic induction heating. Additionally, we assessed the efficiency of copper ferrite nanoparticles in methylene blue degradation and found that they exhibit higher efficiency at high temperatures in comparison with iron ferrite.<sup>20</sup> Building upon this groundwork, our current research delves deeper into the intrinsic properties of various metal ferrite nanoparticles for free radical production and explores the influence of different parameters of the nanocatalyst system. By doing so, we aim to tailor each nanocatalyst according to specific application requirements considering a highly reproducible microwave-assisted polyol method.

In this study, we focused on Mn, Zn, and Co dopants due to their distinct redox behaviors and contrasting influence on ROS generation. This selection enabled a mechanistic comparison beyond pollutant degradation, highlighting how each dopant modulates radical type and reactivity under standardized conditions.

## 2. Materials and methods

### 2.1 Chemical reagents and analysis

Reagents such as iron(II) acetate ( $\text{FeAc}_2$ ,  $\geq 99.99\%$ ), cobalt(II) acetate ( $\text{CoAc}_2$ ,  $99.99\%$ ), manganese(II) acetate ( $\text{MnAc}_2$ ,  $98\%$ ), zinc acetate ( $\text{ZnAc}_2$ ,  $99.99\%$ ), diethylene glycol (DEG,  $99\%$ ),

nitric acid ( $\text{HNO}_3$ ,  $65\%$ ), iron(III) nitrate nonahydrate ( $\text{Fe}(\text{NO}_3)_3 \cdot 9\text{H}_2\text{O}$ ,  $95\%$ ) ethanol ( $99.8\%$ ), 5,5-dimethyl-1-pyrroline *N*-oxide (DMPO,  $\geq 97\%$ ), dimethyl sulfoxide (DMSO,  $>99\%$ ), hydrogen peroxide ( $\text{H}_2\text{O}_2$ ,  $30\%$ ), and methylene blue (MB,  $\geq 82\%$ ) were purchased from Sigma Aldrich.

The iron and transition metals' concentrations in the colloidal suspensions of ferrite nanocatalysts were analyzed using inductively coupled plasma optical emission spectroscopy (ICP-OES) with a PerkinElmer OPTIME 2100DV apparatus. Samples were digested overnight with aqua regia at  $90^\circ\text{C}$ .

The degradation of MB was monitored using colorimetric measurements with a PerkinElmer LAMBDA 35 UV-visible spectrophotometer following a characteristic band at a wavelength of  $663\text{ nm}$ . A calibration curve of absorbance versus concentration was established by measuring the absorbance of MB dilutions ranging from  $0.5$  to  $5\text{ ppm}$ .

### 2.2 Synthesis

The metal ferrite nanocatalysts were synthesized according to a previously described microwave-assisted polyol procedure in a microwave oven Monowave 300® (Anton Paar GmbH, Graz, Austria) working at  $2.45\text{ GHz}$ .<sup>16,21</sup> Briefly,  $300\text{ mg}$  of  $\text{FeAc}_2$  was dispersed in  $18.3\text{ mL}$  of DEG and  $0.7\text{ mL}$  of  $\text{H}_2\text{O}$  in a G30 glass vial with a magnetic stirrer. The vial was placed in the microwave reactor, stirred at  $600\text{ rpm}$ , and heated at  $3.75^\circ\text{C min}^{-1}$  to  $170^\circ\text{C}$ , where it was maintained for  $2\text{ h}$  before rapidly cooling to  $55^\circ\text{C}$ . The product was separated by centrifugation at  $8000\text{ rpm}$  for  $45\text{ min}$ , and the dark precipitate was washed three times with ethanol by centrifugation at  $8000\text{ rpm}$  for  $15\text{ min}$  each. The final product was dried under air flow and redispersed in distilled water. This first sample was labeled MW- $\text{Fe}_3\text{O}_4$ .

The same protocol was used to synthesize smaller-sized particles and manganese, cobalt, and zinc ferrite nanocatalysts. To reduce the particle size, the only change was the amount of water, using  $0.4\text{ mL}$  instead, leading to the sample MW- $\gamma\text{-Fe}_2\text{O}_3$ - $8\text{ nm}$ . For the metal ferrites,  $\text{MnAc}_2$ ,  $\text{Co}(\text{Ac})_2$ , and  $\text{Zn}(\text{Ac})_2$  were added to the reaction mixture in a weight ratio of  $\text{Fe}/\text{M} = 2$ , where M represents the divalent cations of the transition metals. Samples were labeled as MW- $\text{M}_x\text{Fe}_{3-x}\text{O}_4$ , with M being the corresponding divalent cation and X estimated from the elemental analysis.

The sample MW- $\text{Fe}_3\text{O}_4$  was subjected to two different oxidation treatments: the first one leaving the sample in aqueous suspension for 6 months (MW- $\gamma\text{-Fe}_2\text{O}_3$ - $14\text{ nm}$ -air) and the second one following an acidic and oxidizing treatment previously described (MW- $\gamma\text{-Fe}_2\text{O}_3$ - $14\text{ nm}$ -AT).<sup>22</sup> Briefly,  $100\text{ mg}$  of the sample was mixed with  $10\text{ mL}$  of  $2\text{ M HNO}_3$  and magnetically stirred for  $15\text{ min}$ . The sample was then magnetically separated, and the supernatant discarded. Next, the sample was mixed with  $5\text{ mL}$  of  $1\text{ M Fe}(\text{NO}_3)_3$  solution, magnetically stirred, heated, and maintained at  $90^\circ\text{C}$  for  $30\text{ min}$ . The sample was then magnetically separated and redispersed in  $10\text{ mL}$  of  $2\text{ M HNO}_3$ , followed by  $15\text{ min}$  of magnetic stirring. Finally, the sample was washed three times with acetone via magnetic separation and redispersed in distilled water.



### 2.3 Characterization

The morphological characteristics of the metal ferrite samples were investigated using transmission electron microscopy (TEM) with a JEOL JEM 1010 at 100 keV. The sample suspensions were deposited onto amorphous carbon-coated copper grids and evaporated at room temperature for sample preparation. About 200 particles were measured to determine the mean particle size and distribution, focusing on their largest internal dimension. X-ray diffraction (XRD) analysis, conducted with a Bruker D8 Advance diffractometer using  $\text{CuK}\alpha$  radiation, identified the phase and crystal structure in the  $2\theta$  range of  $20^\circ$  to  $70^\circ$ . The mean crystal size was estimated using Scherrer's equation based on the full width at half-maximum of the most intense peak (311).

The colloidal characteristics of the nanocatalysts were assessed using dynamic light scattering (DLS) on a Zetasizer Nano SZ system (Malvern Instruments, UK), which operates with a solid-state He-Ne laser ( $\lambda = 633 \text{ nm}$ ). Measurements of the hydrodynamic diameter were carried out at pH 7, reporting the mean particle size based on the intensity distribution. Additionally,  $\zeta$ -potential values were determined across a range of pH levels, adjusted with KOH or  $\text{HNO}_3$  and using  $10^{-3} \text{ M KNO}_3$  as the background electrolyte.

Thermal analysis (TGA/DSC) was performed using a TA Instrument Q2000 differential scanning calorimeter, heating in air at  $10 \text{ }^\circ\text{C min}^{-1}$  up to  $800 \text{ }^\circ\text{C}$ , to measure the weight loss associated with DEG presence. Fourier-transform infrared spectroscopy (FTIR) in the range of  $400\text{--}4000 \text{ cm}^{-1}$  was employed to further analyze the composition of the samples.

The magnetic behavior of the samples was analyzed using a LakeShore 7300 vibrating sample magnetometer (VSM). Hysteresis loops were recorded at 290 K by applying magnetic fields in the range of  $\pm 790 \text{ kA m}^{-1}$ , from which the saturation magnetization ( $M_s$ ) and coercivity ( $H_c$ ) and the remanent magnetization ( $M_R$ ) were computed.

X-ray photoelectron spectroscopy (XPS) has been used to characterize the elemental composition and the oxidation states of Fe, Mn and Zn present on the surface of the samples. The XPS experiments were performed in an UHV chamber with a base pressure of  $10\text{--}10 \text{ mbar}$  equipped with a hemispherical electron energy spectrometer (Phoibos 150, SPECS Surface Nano Analysis GmbH, Germany) and a 2D delay-line detector (Surface Concept GmbH, Germany), using an X-ray source of Al-K $\alpha$  ( $1486.6 \text{ eV}$ ).<sup>23</sup> The XPS spectra were acquired at normal emission take-off angle, using an energy step of 0.50 and 0.10 eV and a pass-energy of 40 and 20 eV for survey spectra and detailed core level regions, respectively. The surface charging effect built up upon the photoemission experiments was compensated using a low energy electron flood gun. The absolute binding energies of the photoelectron spectra were determined by referencing to the C 1s photoelectron peak at  $285.0 \text{ eV}$ . Both peak energy and line shape of the C 1s peak were checked before and after the measurement of every selected core level transition. The spectra were analyzed with the CasaXPS program (Casa Software Ltd, Cheshire,

UK) using a Shirley method for background subtraction and data processing for quantitative XPS analysis. The spectra are displayed after the subtraction of the contribution of the Al-K $\alpha$  satellite emission.

### 2.3 Evaluation of the catalytic activity

The generation of free radicals by the catalysts was analyzed using EPR in the X-band (9.5 GHz) at room temperature with a BRUKER ELEXSYS II-E500 spectrometer, employing DMPO as a spin trap in DMSO ( $0.17 \text{ g mL}^{-1}$ ). DMSO was used only to better solubilize DMPO, allowing a better dispersion of the spin trap, and was carefully considered in data interpretation. Measurements were conducted with a modulation signal of 100 kHz and 3 G amplitude, using the stable resonance area of  $\text{Mn}^{2+}$  radicals in a MgO crystal ( $\text{MgO:Mn}^{2+}$ ) as a reference signal to normalize free radical production, which allows comparison of intensities between samples. For the experiments,  $0.1 \text{ mg mL}^{-1}$  of catalyst was dispersed in  $200 \text{ }\mu\text{L}$  of acetate buffer (pH 4.8) in a quartz tube with a measurement region height of 30 mm. Then,  $50 \text{ }\mu\text{L}$  of DMPO/DMSO solution was added, followed by  $10 \text{ }\mu\text{L}$  of  $\text{H}_2\text{O}_2$  aqueous solution (30%). The EPR spectra were recorded at intervals of 10 min. The collected data were analyzed using the software Spinfit from Bruker, allowing a fitting procedure that considered the contribution of different radicals with hyperfine parameters assigned according to the database <https://tools.niehs.nih.gov/stdb/index.cfm/spintrap/>.

To evaluate the catalytic activity of the nanocatalyst based on the type of free radical, MB degradation assays were conducted. Nanocatalyst samples ( $1 \text{ mg mL}^{-1}$  in the final mixture) were mixed with 10 mL of 100 ppm MB at pH 5. These concentrations were selected based on prior optimization to ensure measurable degradation kinetics while maintaining nanoparticle colloidal stability.<sup>16,17</sup> Before initiating the oxidation process, MB adsorption was allowed to reach equilibrium over 2 h. Degradation commenced with the addition of  $100 \text{ }\mu\text{L}$  of  $\text{H}_2\text{O}_2$  (30%). Kinetic data were obtained by measuring the MB solution at various contact times (0, 5, 15, 30, 60, 180, and 1440 min) after retrieving the nanocatalysts *via* magnetic separation.

## 3. Results and discussion

### 3.1. Synthesis and reproducibility of iron oxide nanoparticles

In this study, a microwave-assisted polyol method was utilized to prepare various metal ferrite nanoparticles. Initially, iron oxide nanoparticles with a narrow size distribution were synthesized following an optimized protocol. The inclusion of water in the reaction mixture reduced the boiling point of the polyol to  $170 \text{ }^\circ\text{C}$ , facilitating the growth of particles to an average size of  $14 \pm 3 \text{ nm}$ , as shown in Fig. 1a and b, with their narrow size distribution illustrated in Fig. 1c.<sup>21,24</sup> Additionally, the use of DEG as a solvent, reducing agent, and surfactant resulted in a slight coating on the iron oxide nanoparticles, referred to as MW- $\text{Fe}_3\text{O}_4$ , which is visible as a less contrasted





**Fig. 1** Structural, compositional and colloidal characterization of the first batch of MW-Fe<sub>3</sub>O<sub>4</sub> (batch 2–8 characterization is shown in the ESI<sup>†</sup>). (a) and (b) TEM images, (c) particle size distribution, (d) X-ray diffraction pattern, (e) hydrodynamic size in intensity, (f) zeta potential (the solid line is a guide to the eye), (g) thermal gravimetric analysis and (h) infrared spectra.

layer in the magnified TEM image (Fig. 1b). XRD analysis (Fig. 1d) confirmed that the iron oxide phase exhibits an inverse spinel structure, characteristic of either magnetite or maghemite, with a crystal size of 14 nm.

The sample's colloidal characteristics indicated a hydrodynamic size of 130 nm and a polydispersity index of 0.2 when dispersed at pH 5 (Fig. 1e). The isoelectric point was found to be at pH 7 (the solid line is a guide for the eyes), reflecting the lack of additional coatings except for the DEG present on the surface, which comprised less than 6%, as shown by TGA analysis (Fig. 1g). Infrared spectroscopy (Fig. 1h) revealed bands at 630 and 410 cm<sup>-1</sup> characteristic of the Fe–O stretching from Fe<sub>3</sub>O<sub>4</sub>, while a band at 1070 cm<sup>-1</sup> was attributed to the DEG molecules. The band at 1620 cm<sup>-1</sup> indicated the C=O stretching vibrations of iron-coordinated carboxylates,<sup>25</sup> and the band at 3400 cm<sup>-1</sup> was associated with surface OH groups and residual water molecules.

Magnetic characterization images of MW-Fe<sub>3</sub>O<sub>4</sub> at 290 K are displayed in Fig. S1,<sup>†</sup> with its corresponding magnetic parameters in Table S1.<sup>†</sup> MW-Fe<sub>3</sub>O<sub>4</sub> exhibited a saturation magnetization ( $M_S$ ) of 78 Am<sup>2</sup> kg<sup>-1</sup> and a low coercive field ( $H_C = 17.8$  Oe). The remanent-to-saturation magnetization ratio ( $M_R/M_S$ ) of 0.051 indicates that approximately 5.1% of the total magnetization is retained after removal of the external magnetic field, which could indicate a predominance of nanoparticles in a superparamagnetic-like regime at this temperature, typical in this sized single core nanoparticles.<sup>26</sup>

To assess the reproducibility of MW-Fe<sub>3</sub>O<sub>4</sub>, eight synthesis batches were performed utilizing the automated arm robot and carousel within the Anton Paar® Monowave microwave. In this sense, the same protocol was followed for each synthesis, preparing all of them at the same time and placing them on the carousel that automatically performed each batch. Detailed characterization of all synthesis can be found in Fig. S2–S4 in the ESI,<sup>†</sup> while Fig. 2 summarizes the reproducibility of the samples in terms of their structural and colloidal parameters, as well as their magnetic properties.

The reproducibility of the structural, colloidal, and magnetic properties of MW-Fe<sub>3</sub>O<sub>4</sub> was consistently high across 8 independent batches, with variations confined to a narrow range and typically above 90%. These batches were synthesized using an automated platform capable of processing up to 30 samples in parallel under identical conditions, which facilitates high-throughput optimization and supports the robustness of the method. While large-scale production was not attempted, this reproducibility represents a promising starting point for future efforts toward continuous or larger-scale synthesis as shown in our recent work on the continuous-flow microwave-assisted oxidative precipitation of iron oxides.<sup>27</sup>

Furthermore, it is important to note that the entire reaction process, including initial heating, spans up to 3 h. During this period, the samples prepared at the start and left in the carousel remained stable and unoxidized, as any alteration in the mixture could prevent particle formation. Consequently, our



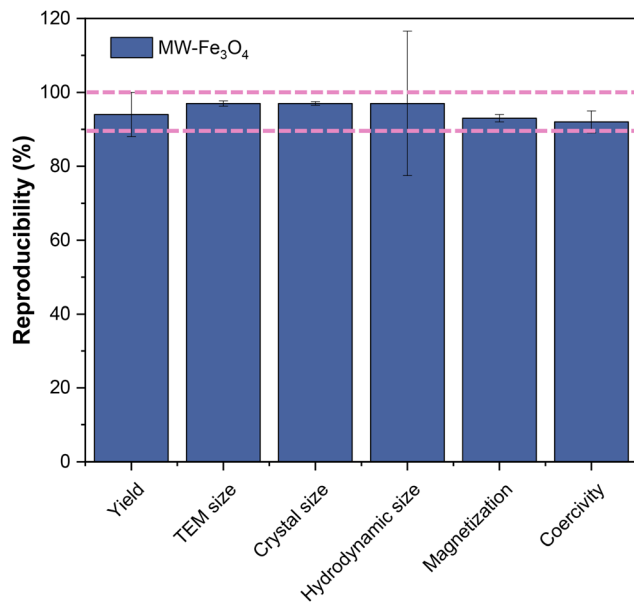


Fig. 2 Reproducibility of MW-Fe<sub>3</sub>O<sub>4</sub> (Z = 8).

findings confirm that the initial sample mixture exhibits remarkable stability before and after the reaction.

The XRD patterns (Fig. S3†) and hydrodynamic size distributions (Table S2†) provided further evidence of the reproducibility of each sample. All samples displayed an inverse spinel structure, similar to magnetite or maghemite (with a lattice parameter of  $8.364 \pm 0.001$ ) and comparable hydrodynamic sizes. Table S2† presents the crystal size and hydrodynamic size relative to the TEM size. Remarkably, the reproducibility rates for the TEM particle size, crystal size, and hydrodynamic size were of 97% for all cases, demonstrating that these parameters can be reliably replicated for this synthetic procedure. Furthermore, the consistency of the magnetic properties (Fig. S4†) and yield (Table S2†) between all samples is very impressive with 93% reproducibility. All samples exhibited nearly superparamagnetic behavior at the measured temperature considering whole particles, with similar coercive fields and a high magnetic moment.

### 3.2 Free radical formation

To assess the catalytic activity of MW-Fe<sub>3</sub>O<sub>4</sub>, EPR spectroscopy was first conducted at room temperature in an acetate buffer (pH 5). The formation kinetics of free radicals was monitored using the spin-trap DMPO in DMSO. Fig. 3 shows the EPR spectra obtained under these conditions, along with the corresponding fitting and deconvolution of the DMPO-adduct radical components. The EPR spectra revealed the presence of four distinct paramagnetic species: (1) <sup>•</sup>OH radicals generated from Fe<sup>2+</sup>, (2) <sup>•</sup>CH<sub>3</sub> radicals likely arising from secondary reactions between the oxygen-based radicals with DMSO, which was used to dilute DMPO, and DEG or acetate molecules,<sup>28</sup> (3) <sup>•</sup>OOH radicals resulting from Fe<sup>3+</sup>, and (4) <sup>•</sup>N<sub>2</sub> radicals related to some decomposition of DMPO and that is also

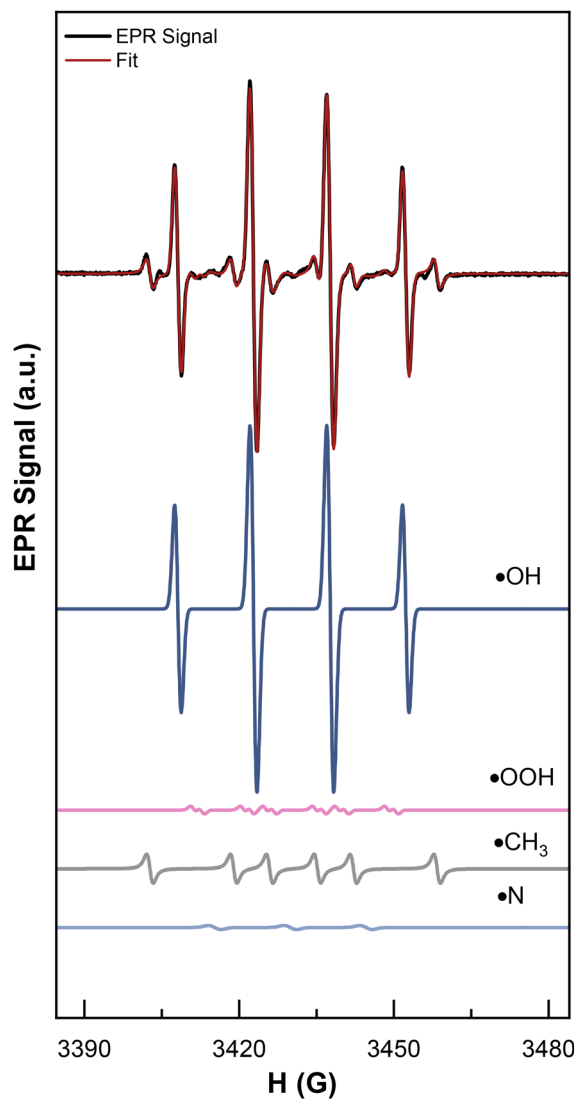


Fig. 3 EPR spectrum and the corresponding fitting of the MW-Fe<sub>3</sub>O<sub>4</sub> sample in the presence of DMPO/DMSO, measured 5 minutes after the addition of H<sub>2</sub>O<sub>2</sub> at room temperature at pH 5. The fitted spectra include the DMPO-adduct radical components presented below.

present in the control solution (*i.e.* without the nanoparticles). To further analyze the free radical formation, it is possible to extract corresponding areas of each DMPO-adduct from the EPR spectra. For comparison purposes, this latter will be discussed in the next section together with the effect of the buffer during the measurement and the oxidation state of the sample MW-Fe<sub>3</sub>O<sub>4</sub>.

**3.2.1 Effect of the buffer and oxidation.** To investigate the influence of the buffer and the oxidation state on the free radical production, three representative samples were selected from those synthesized in this study: (1) MW-Fe<sub>3</sub>O<sub>4</sub>, (2) MW- $\gamma$ -Fe<sub>2</sub>O<sub>3</sub> oxidized in air, and (3) MW- $\gamma$ -Fe<sub>2</sub>O<sub>3</sub> oxidized under acidic conditions. The successful oxidation of MW-Fe<sub>3</sub>O<sub>4</sub> was confirmed by infrared spectroscopy, as shown in Fig. S5.† In addition to the characteristic bands of water ( $\sim 3400$  cm<sup>-1</sup>) and



DEG ( $\sim 1070\text{ cm}^{-1}$ ), the Fe–O stretching region shows a noticeable broadening, with the emergence of new absorption bands at  $640$  and  $400\text{ cm}^{-1}$ , which are consistent with the formation of  $\gamma\text{-Fe}_2\text{O}_3$  (maghemite). Furthermore, upon oxidation to maghemite (MW- $\gamma\text{-Fe}_2\text{O}_3$ ),  $M_S$  decreased to  $51\text{ Am}^2\text{ kg}^{-1}$ , and the  $H_C$  dropped sharply to  $0.99\text{ Oe}$ , confirming the transition toward a more thermally unstable (superparamagnetic-like) state (see Fig. S1 and Table S1†) due to reduced magnetic anisotropy. This reduction in magnetic response is attributed to the structural and electronic changes associated with the oxidation process. In particular, the conversion of  $\text{Fe}^{2+}$  to  $\text{Fe}^{3+}$  alters the cation distribution within the spinel lattice and reduces the net magnetic moment, as maghemite contains only  $\text{Fe}^{3+}$  ions. Additionally, the formation of cation vacancies during oxidation introduces structural disorder, which further disrupts magnetic exchange interactions and lowers the effective magnetic anisotropy. As a result, the energy barrier for moment reorientation decreases, allowing thermal fluctuations at room temperature to overcome it more easily, thus promoting superparamagnetic relaxation.<sup>29</sup>

Free radical formation was investigated through various experimental conditions, as illustrated in Fig. 4a–d. When the MW- $\text{Fe}_3\text{O}_4$  sample was measured in an acetate buffer solution (Fig. 4a), a significant production of  $\cdot\text{OH}$  radicals was observed. The buffer likely stabilizes the MW- $\text{Fe}_3\text{O}_4$  particles, facilitating effective redox cycling and prompting  $\cdot\text{OH}$  radical generation. This observation aligns with previous findings where magnetite nanoparticles exhibit high catalytic activity, particularly in environments that favor redox reactions.<sup>11</sup> In contrast, MW- $\gamma\text{-Fe}_2\text{O}_3$ -air measured in buffer (Fig. 4b) predominantly produced  $\cdot\text{CH}_3$  radicals. This phenomenon can be attributed to a secondary reaction between the  $\cdot\text{OOH}$  with DMSO and the acetate buffer, suggesting that the buffer composition can influence the nature of the detected radicals.<sup>28,30</sup> This unexpected detection of methyl radicals ( $\cdot\text{CH}_3$ ) in the EPR spectra of MW- $\gamma\text{-Fe}_2\text{O}_3$ -air in the presence of acetate buffer suggests that the buffer itself is not chemically inert under these experimental conditions. Instead, it appears to actively participate in side reactions that modify the radical profile detected by spin trapping. When the production of oxygen-based radical is higher, then the detection of  $\cdot\text{CH}_3$  radicals is favored in comparison with a lower production, where the previous reaction of  $\cdot\text{OOH}$  with the organic component of the buffer is more probable than with DMSO.

To verify this hypothesis, MW- $\gamma\text{-Fe}_2\text{O}_3$ -air was measured without the buffer by controlling the pH with diluted HCl (Fig. 4c). The resulting EPR spectra confirmed the presence of  $\cdot\text{OOH}$  radicals, as expected due to the presence of  $\text{Fe}^{3+}$  only.<sup>31</sup> By eliminating the buffer, the true nature of the radical species generated by MW- $\gamma\text{-Fe}_2\text{O}_3$ -air could be discerned, revealing that  $\cdot\text{OOH}$  radicals are inherently produced in the absence of interfering substances and that the detection of  $\cdot\text{CH}_3$  adducts points to a deviation from the expected radical generation pathway. A plausible mechanism involves the reaction of acetate anions ( $\text{CH}_3\text{COO}^-$ ) with  $\cdot\text{OOH}$  radicals, which are moderately oxidizing and capable of abstracting hydrogen atoms.



**Fig. 4** Effect of the buffer and the oxidation of the NPs on the free radical formation measured at pH = 4.8. (a)  $\text{Fe}_3\text{O}_4$  in buffer, (b) MW- $\gamma\text{-Fe}_2\text{O}_3$ -air in buffer, (c) MW- $\gamma\text{-Fe}_2\text{O}_3$ -air measured without buffer and (d) MW- $\gamma\text{-Fe}_2\text{O}_3$  oxidized by an acidic treatment (AT) measured without buffer.

Although less reactive than  $\cdot\text{OH}$ ,  $\cdot\text{OOH}$  can still engage in proton-coupled electron transfer or hydrogen abstraction processes, particularly in the presence of transition metal ions or under microwave stimulation that increases the energy of the system. However, such interference is not observed when  $\cdot\text{OH}$  radicals are generated, suggesting that the formation of  $\cdot\text{CH}_3$  is not due to direct oxidation of acetate alone. This discrepancy implies that  $\cdot\text{OOH}$  may engage in intermediate steps involving the surface of the nanoparticle, DMSO, or other transient species present in the medium, leading indirectly to  $\cdot\text{CH}_3$  formation. The acetate buffer may facilitate or stabilize these intermediates, promoting reaction pathways that are otherwise suppressed in its absence.

Furthermore, the sample of MW- $\gamma\text{-Fe}_2\text{O}_3$ -AT, oxidized by an acidic treatment (Fig. 4d), showed no free radical production, likely due to the presence of nitrate ions from the treatment (infrared spectra Fig. S5†). These nitrate ions might form a passivating layer on the particle surface, inhibiting radical formation. In this sense, it can be inferred that surface chemistry



plays a critical role in the catalytic behavior of MW- $\gamma$ -Fe<sub>2</sub>O<sub>3</sub>, and the presence of specific surface groups can significantly alter the particle's reactivity inhibiting catalytic processes.

**3.2.2 Effect of the particle size.** Understanding how particle size influences radical formation is crucial for optimizing these materials for specific catalytic applications, where the efficiency of radical generation plays a significant role. In this sense, we compare the free radical formation between MW-Fe<sub>2</sub>O<sub>3</sub>-air of 14 nm with a smaller-sized sample MW- $\gamma$ -Fe<sub>2</sub>O<sub>3</sub>-8 nm. The latter was synthesized by reducing the amount of water in the microwave-assisted polyol process leading to a notable decrease in the particle size as can be appreciated in the TEM image of MW- $\gamma$ -Fe<sub>2</sub>O<sub>3</sub>-8 nm at Fig. 5a. Fig. 5b shows the corresponding particle size distribution with a mean particle size of  $8 \pm 2$  nm. Additionally, the XRD pattern in Fig. 5c indicates that the iron oxide phase maintains an inverse spinel structure, characteristic of magnetite or maghemite, with a crystal size of approximately 8 nm. Furthermore, MW- $\gamma$ -Fe<sub>2</sub>O<sub>3</sub>-8 nm exhibited a markedly diminished magnetic response compared to its larger counterpart (see Fig. S1 and Table S1†). At 290 K, it displayed a  $M_S$  of  $48 \text{ Am}^2 \text{ kg}^{-1}$  and an extremely low  $H_C$  of 0.63 Oe, indicative of superparamagnetic behavior. Notably, the remanent-to-saturation magnetization ratio was only 0.002, confirming that no net magnetization is retained after removal of the external magnetic field.

Fig. 5d illustrates the comparison of  $\cdot\text{OOH}$  radical production between the 14 nm and 8 nm MW- $\gamma$ -Fe<sub>2</sub>O<sub>3</sub> samples (controlling the pH with diluted HCl). The data reveal that the smaller-sized nanoparticles produce a larger quantity of  $\cdot\text{OOH}$  radicals. This enhanced radical production can be attributed to the increased surface area resulting from the reduced particle size, as also proved in other catalytic systems.<sup>32</sup> Smaller nanoparticles have a higher surface-to-volume ratio, providing more active sites for catalytic reactions, which in turn facilitates greater radical generation. The ability to precisely control and confirm the size and structure of these nanoparticles is

essential for correlating their physical properties with their catalytic activity.

**3.2.3 Effect of transition metals.** For catalytic applications, the varying effects of transition metals underscore the importance of careful selection and optimization of dopants to tailor the catalytic properties of ferrite nanoparticles. In this sense, the effect of transition metal doping on the formation of  $\cdot\text{OOH}$  radicals in ferrite nanoparticles was examined by incorporating manganese (MW-Mn<sub>0.4</sub>Fe<sub>2.6</sub>O<sub>4</sub>), zinc (MW-Zn<sub>0.7</sub>Fe<sub>2.3</sub>O<sub>4</sub>) and cobalt (MW-Co<sub>0.5</sub>Fe<sub>2.5</sub>O<sub>4</sub>). The chemical composition of each doped sample was determined through ICP-OES measurements. The TEM images of the doped ferrite nanoparticles are shown in Fig. 6a–c, respectively, and the particle size distribution is shown in Fig. 6d. Interestingly, the incorporation of manganese and cobalt resulted in a reduction in the particle size to 7 nm, which can be attributed to a lower bond energy of the added ions compared to the removed ions.<sup>33</sup> This reduction in size observed in MW-Mn<sub>0.4</sub>Fe<sub>2.6</sub>O<sub>4</sub> and MW-Co<sub>0.5</sub>Fe<sub>2.5</sub>O<sub>4</sub> likely enhances the catalytic activity due to the increased surface area and high crystallinity, as indicated by the X-ray diffraction patterns (Fig. 6e). On the other hand, the slight increase in size for MW-Zn<sub>0.7</sub>Fe<sub>2.3</sub>O<sub>4</sub> suggests a different interaction mechanism between Zn ions and the iron oxide lattice, which might influence the catalytic properties differently. Furthermore, Table 1 displays a summary with the structural parameters of the as-prepared metal ferrite nanoparticles, including the lattice parameters.

As can be seen for the doped nanoparticles, there is an increase in this lattice parameter (Fe < Co < Mn < Zn) which implies an expansion due to the replacing of Fe ions in the ferrite structure, similarly observed in our previous work and by other researchers.<sup>21,34,35</sup>

This cation substitution has a marked effect on the magnetic properties of the samples (Fig. S1 and Table S1†). MW-Mn<sub>0.4</sub>Fe<sub>2.6</sub>O<sub>4</sub> exhibited an  $H_C$  value of 8.8 Oe and a low  $M_R/M_S$  ratio (0.013), suggesting partial blocking and relatively



Fig. 5 Effect of the size on the  $\cdot\text{OOH}$  radical formation measured at pH 4.8 adjusted with diluted HCl. (a) TEM image, (b) particle size distribution and (c) X-ray diffraction pattern of MW- $\gamma$ -Fe<sub>2</sub>O<sub>3</sub>-8 nm. (d)  $\cdot\text{OOH}$  production of MW- $\gamma$ -Fe<sub>2</sub>O<sub>3</sub>-8 nm compared to the one of MW- $\gamma$ -Fe<sub>2</sub>O<sub>3</sub> of 14 nm.





**Fig. 6** Effect of the metal doping of ferrite nanoparticles on the formation of  $\cdot\text{OOH}$  radicals. TEM images of (a) MW- $\text{Co}_{0.5}\text{Fe}_{2.5}\text{O}_4$ , (b) MW- $\text{Zn}_{0.7}\text{Fe}_{2.3}\text{O}_4$  and (c) MW- $\text{Mn}_{0.4}\text{Fe}_{2.6}\text{O}_4$ . (d) particle size distribution, (e) X-ray diffraction patterns of metal ferrite nanoparticles and (f)  $\cdot\text{OOH}$  radical formation. MW- $\text{Co}_{0.5}\text{Fe}_{2.5}\text{O}_4$  (orange), MW- $\text{Zn}_{0.7}\text{Fe}_{2.3}\text{O}_4$  (light blue) and MW- $\text{Mn}_{0.4}\text{Fe}_{2.6}\text{O}_4$  (purple).

**Table 1** Structural parameters of metal ferrite nanoparticles

Sample	TEM size (nm)	Crystal size (nm)	Lattice parameter ( $\text{\AA}$ )
MW- $\text{Fe}_3\text{O}_4$	$14 \pm 3$	$14.1 \pm 0.3$	$8.364 \pm 0.001$
MW- $\gamma\text{-Fe}_2\text{O}_3$ 8 nm	$8 \pm 2$	$8.2 \pm 0.2$	$8.368 \pm 0.042$
MW- $\text{Mn}_{0.4}\text{Fe}_{2.6}\text{O}_4$	$7 \pm 2$	$6.4 \pm 0.2$	$8.417 \pm 0.043$
MW- $\text{Zn}_{0.7}\text{Fe}_{2.3}\text{O}_4$	$16 \pm 5$	$14.5 \pm 0.4$	$8.438 \pm 0.037$
MW- $\text{Co}_{0.5}\text{Fe}_{2.5}\text{O}_4$	$7 \pm 2$	$7.3 \pm 0.3$	$8.395 \pm 0.003$

low effective anisotropy. Zn substitution further softened the magnetic response with very low  $H_C$  (5.2 Oe) and an  $M_R/M_S$  value of 0.016, indicating near-superparamagnetic behavior even at 14 nm. In contrast, Co substitution led to the highest coercivity (83.0 Oe) and remanence ratio (0.108), confirming the known effect of  $\text{Co}^{2+}$  in enhancing magnetic anisotropy.

Fig. 6f compares the  $\cdot\text{OOH}$  radical production for the three metal-doped ferrite samples. Manganese doping appears to significantly enhance  $\cdot\text{OOH}$  radical production, suggesting that  $\text{Mn}^{2+}$  ions in the iron oxide lattice facilitate the generation

of reactive oxygen species. Similar EPR studies on manganese ferrite nanoparticles also exhibited that the main ROS produced by this kind of material are  $\cdot\text{OOH}$  radicals.<sup>36,37</sup> This enhancement could be due to the unique electronic configuration of manganese, which might promote redox reactions more effectively than iron alone. In other words,  $\text{Mn}^{2+}$  can be easily oxidized to higher oxidation states and undergo redox cycling between different oxidation states (e.g.,  $\text{Mn}^{2+}$  to  $\text{Mn}^{3+}$  and back).<sup>38</sup> This cycling can generate ROS as a byproduct, particularly the  $\cdot\text{OOH}$  radicals, which play a crucial role in complementing the direct electron-transfer mechanism in the reactivity of manganese oxides.<sup>39</sup>

Conversely, Zn-doping completely inhibits the production of free radicals, suggesting a possible passivation effect where Zn ions stabilize the lattice, reducing the formation of reactive intermediates. Zinc typically exists in a stable +2 oxidation state ( $\text{Zn}^{2+}$ ), which does not readily participate in redox reactions. Unlike transition metals such as iron,<sup>40</sup> copper,<sup>41</sup> or manganese,<sup>36</sup> which can cycle between different oxidation states and facilitate ROS generation through redox reactions, zinc remains in its stable state.<sup>42</sup> This stability reduces its like-



likelihood of contributing to ROS formation. In its +2 oxidation state, zinc has a full  $d^{10}$  electron configuration, meaning it lacks unpaired electrons and, therefore, does not easily engage in the redox reactions necessary for ROS production.<sup>43</sup> Metals that generate ROS typically have unpaired d electrons that interact with oxygen or other molecules to form radicals. Furthermore, the increase in the particle size of MW-Zn<sub>0.7</sub>Fe<sub>2.3</sub>O<sub>4</sub> may be attributed to an enrichment of Zn on the surface of the particles (see section 3.3 Surface analysis). This occurs because the preferential electronic configuration for tetrahedral bonding with Zn<sup>2+</sup> ions in the spinel lattice is not perfectly aligned, leading to some distortion that can contribute to an external phase crystallization, which may passivate the surface of the nanoparticles.<sup>44</sup> Therefore, the passivation layer can prevent the active sites on the nanoparticle surface from participating in redox reactions that generate ROS.

Cobalt doping, on the other hand, results in a reduction of half  $\cdot$ OOH radical concentration compared to MW- $\gamma$ -Fe<sub>2</sub>O<sub>3</sub>-8 nm, though not as drastically as zinc. This suggests that cobalt ions partially inhibit radical formation, possibly due to

competing redox reactions or a change in the electronic environment that affects the availability of active sites for  $\cdot$ OOH radical production.

### 3.3 Surface analysis

Fig. 7 summarizes the detailed surface analysis of the samples by XPS to further support the abovementioned findings on free radical production. Specifically, Fig. 7a displays the energy region of the Fe 2p spectra corresponding to the MW-Fe<sub>3</sub>O<sub>4</sub>, MW- $\gamma$ -Fe<sub>2</sub>O<sub>3</sub>-air, MW- $\gamma$ -Fe<sub>2</sub>O<sub>3</sub>-AT samples. The spectra were normalized to the maximum intensity to highlight line shape differences, which provides direct valuable insights into the Fe oxidation states. All samples show a photoelectron emission with a complex line shape mainly dominated by two wide peaks corresponding to the spin-orbit 3/2 and 1/2 doublet. Once spectra are normalized to the maximum intensity, there are no line shape differences between them. Therefore, they are equivalent in terms of Fe oxidation states present. Upon comparison, with standard iron oxide compounds, of the binding energy positions of both peaks, their energy splitting



**Fig. 7** Surface analysis by XPS. (a) XPS spectra of Fe 2p corresponding to the MW-Fe<sub>3</sub>O<sub>4</sub>, MW- $\gamma$ -Fe<sub>2</sub>O<sub>3</sub>-air, MW- $\gamma$ -Fe<sub>2</sub>O<sub>3</sub>-AT samples. The XPS spectra were normalized to maximum peak intensity for better visual inspection and direct comparison between the samples. (b) Normalized XPS spectra of Fe 2p corresponding to the MW-Mn<sub>0.4</sub>Fe<sub>2.6</sub>O<sub>4</sub> and MW-Zn<sub>0.7</sub>Fe<sub>2.3</sub>O<sub>4</sub> samples. (c) XPS spectrum of Fe 2p corresponding to the MW-Zn<sub>0.7</sub>Fe<sub>2.3</sub>O<sub>4</sub> sample. Data points are represented as black solid symbols, Shirley background as dotted lines and components using solid lines, and the fitting curve as a light blue line. (d) Mn and Fe 3p spectra corresponding to the MW-Mn<sub>0.4</sub>Fe<sub>2.6</sub>O<sub>4</sub> sample. (e) Zn and Fe 3p spectra corresponding to the MW-Zn<sub>0.7</sub>Fe<sub>2.3</sub>O<sub>4</sub> sample. (f) Mn 2p spectra corresponding to the MW-Mn<sub>0.4</sub>Fe<sub>2.6</sub>O<sub>4</sub> sample. (g) Zn 2p spectra corresponding to the MW-Zn<sub>0.7</sub>Fe<sub>2.3</sub>O<sub>4</sub> sample.



and the presence/absence of characteristic satellites, one can determine the oxidation states present.<sup>45,46</sup>

In our case, the analysis of the multiplet structure reveals three weak emissions (grey arrows in Fig. 7a). The first one, which appears between the doublets, is shifted to higher binding energy *ca.* 8.0 eV above the 2p<sub>3/2</sub> component; the others are *ca.* 8.5 and 17.0 eV, respectively, above the 2p<sub>1/2</sub> component. In accordance with the presence of these three emissions and their corresponding binding energy values, together with the energy splitting (13.6 eV) of the major 2p<sub>3/2</sub> and 2p<sub>1/2</sub> peaks, it is suggested that the Fe oxide signal mainly comes from Fe<sup>3+</sup> states.

However, it is important to note that XPS has a surface sensitivity limited to only several nanometers, which must be considered when interpreting the oxidation states.<sup>46</sup> Specifically, Fe<sup>2+</sup> is known to be unstable at the surface, readily oxidizing to Fe<sup>3+</sup> upon exposure to air or even during handling, potentially skewing the measurement toward higher oxidation states.<sup>46</sup> Additionally, EPR measurements conducted on freshly synthesized MW-Fe<sub>3</sub>O<sub>4</sub> reveal the presence of Fe<sup>2+</sup> species, most likely located within the particle core, beyond the surface sensitivity limit of XPS. These Fe<sup>2+</sup> ions can serve as internal electron donors, effectively acting as an ion pump that promotes ·OH radical formation. Under these conditions, the generation of ·OOH radicals—typically associated with surface Fe<sup>3+</sup>—is suppressed due to interference from the buffer used during EPR analysis, which accounts for the exclusive detection of ·OH radicals in the spectra.

Although O 1s spectra were recorded, the strong overlap between lattice oxygen, surface hydroxyl groups, and adsorbed species—whose content varies between samples—hindered a conclusive interpretation. Further deconvolution studies are suggested to elucidate the oxygen-related surface processes.

Fig. 7b displays the comparison of the Fe 2p spectra corresponding to the MW-Mn<sub>0.4</sub>Fe<sub>2.6</sub>O<sub>4</sub> and MW-Zn<sub>0.7</sub>Fe<sub>2.3</sub>O<sub>4</sub> samples, which yield similar results to those shown in Fig. 7a in terms of lineshape, presence of satellites, peak binding energy and splitting values characteristic of the Fe<sup>3+</sup> oxidation state. The XPS spectrum of the Fe 2p core level corresponding to the MW-Zn<sub>0.7</sub>Fe<sub>2.3</sub>O<sub>4</sub> sample is shown in Fig. 7c together with its fit composed of shifted components associated with the spin-orbit 3/2 and 1/2 doublet and the presence of Fe<sup>3+</sup> at octahedral and tetrahedral sublattices *ca.* 2.0 eV apart, and their characteristic shake-up satellite emissions, respectively, using as parameters those obtained from the fit of the ZnFe<sub>2</sub>O<sub>4</sub> reference sample and the binding energy shifts published elsewhere.<sup>46,47</sup> Experimental data points in spectrum are represented as black solid symbols, Shirley background as dotted lines and components using solid lines. The fitting curve (light blue line) resulted from the addition of all those contributions. Note that the XPS spectrum has been vertically shifted for a better visual inspection.

The overall surface elemental composition of the MW-Mn<sub>0.4</sub>Fe<sub>2.6</sub>O<sub>4</sub> and MW-Zn<sub>0.7</sub>Fe<sub>2.3</sub>O<sub>4</sub> samples was derived from the emission of their corresponding 2p and 3p core levels, with different peak intensities (Fig. 7d and 4e), respect-

**Table 2** Relative percentage of elemental content (at%) obtained by XPS analysis for MW-Mn<sub>0.4</sub>Fe<sub>2.6</sub>O<sub>4</sub> and MW-Zn<sub>0.7</sub>Fe<sub>2.3</sub>O<sub>4</sub> samples, and Mn/Fe and Zn/Fe atomic ratios determined from 2p and 3p core level emissions, respectively

Sample	M	M (2p/ 3p)	Fe (2p/ 3p)	M/Fe (2p)	M/Fe (3p)	M/Fe (nominal)
MW-Mn <sub>0.4</sub> Fe <sub>2.6</sub> O <sub>4</sub>	Mn	16.1/ 13.6	83.9/ 86.4	0.19	0.16	0.15
MW-Zn <sub>0.7</sub> Fe <sub>2.3</sub> O <sub>4</sub>	Zn	43.9/ 35.5	56.1/ 64.5	0.78	0.55	0.30

ively). In particular, the Mn/Fe and Zn/Fe ratios were determined by measuring the integral peak areas for each element, after background subtraction and normalization using sensitivity factors provided by electron energy analyzer's manufacturer. According to this, the relative percentage of atomic content is summarized in Table 2.

It is worth noting that for the MW-Mn<sub>0.4</sub>Fe<sub>2.6</sub>O<sub>4</sub> sample the Mn/Fe ratio obtained for the 3p level yields a value close to the nominal one, and a very subtle increase for the 2p level. Photoelectrons emitted from these 2p and 3p states with different binding energy values have very different kinetic energy ranges and, therefore, different probing depths. In particular, 2p peaks provide surface sensitivity since their emission comes mostly from the outermost layers of the samples. Conversely, low binding energy signals from 3p levels with higher kinetic energy are emitted from deeper regions, which significantly enhance the contribution from the inner layers of the nanoparticles, with a minor influence from the outer surface and contaminants. It should be noted that in the case of chemically uniform nanoparticles, these 3p and 2p intensity ratios should be similar. This fact is confirmed for the MW-Mn<sub>0.4</sub>Fe<sub>2.6</sub>O<sub>4</sub> sample, which suggests that Mn is mainly homogeneously distributed in the nanoparticles close to the nominal composition of the ferrite. On the contrary, the calculated Zn/Fe ratio in the MW-Zn<sub>0.7</sub>Fe<sub>2.3</sub>O<sub>4</sub> sample for the 2p level also provides a significantly higher and very distinct value than that one obtained for the 3p state. This result confirms that there exists a clear Zn enrichment on the surface of the nanoparticles. In addition, the relative total content of zinc and iron is not kept constant but superior to the nominal one if it is compared to that one calculated from the 3p emission. Then, the nanoparticles cannot be considered as a uniform system according to XPS depth sensitivity limited to several nanometers. This fact also suggests the existence of a subsurface inner region where there exists a high content of segregated Zn consistent with the formation of a thick and graded Zn-enhanced solid solution shell which might influence on the catalytic activity.

In addition, the study of the Mn and Zn oxidation states requires the analysis of their corresponding 2p core level spectra for the MW-Mn<sub>0.4</sub>Fe<sub>2.6</sub>O<sub>4</sub> and MW-Zn<sub>0.7</sub>Fe<sub>2.3</sub>O<sub>4</sub> samples, respectively. A detailed line shape analysis of the XPS core level spectra is required in order to obtain information on



the Mn oxidation states (Fig. 7f). Upon inspection of Mn 2p, apart from the main doublet peaks corresponding to Mn 2p<sub>3/2</sub> and Mn 2p<sub>1/2</sub>, the appearance of the wide and pronounced shake-up satellite structure at binding energies in the range from 640 to 648 and 655 to 660 eV, respectively, can be seen. These satellite peaks are known to be characteristic of the Mn<sup>2+</sup> phase in agreement with the results reported in the literature.<sup>45,48–50</sup> In addition, a minor shoulder or asymmetry can be inferred on the low binding energy side of the Mn 2p<sub>3/2</sub> peak, which has been reported as a Mn<sup>2+</sup> characteristic feature.<sup>48,50</sup> A further confirmation that enables straightforward identification of Mn oxidation states comes from the analysis of the Mn 3s multiplet splitting (not shown), which value has been correlated in a linear relationship to simple and monovalent oxides such as MnO, Mn<sub>2</sub>O<sub>3</sub>, MnOOH and MnO<sub>2</sub>.<sup>50</sup> In our particular case, Mn 3s multiplet splitting is 6.0 eV approximately and from this large energy splitting one can confirm the majority presence of Mn<sup>2+</sup> in the samples as expected.

Regarding the oxidation state of Zn in the MW-Zn<sub>0.7</sub>Fe<sub>2.3</sub>O<sub>4</sub> sample, the analysis of the Zn 2p energy region shows the appearance of two main peaks at 1021.3 eV and 1044.5 eV that can be ascribed to the Zn 2p<sub>3/2</sub> and the Zn 2p<sub>1/2</sub>, with a doublet separation of 23.2 eV (Fig. 7g). Zn 2p<sub>3/2</sub> and Zn 2p<sub>1/2</sub> emissions can be fitted with only one component each. This result is consistent with the existence of a single chemical environment in the form of Zn<sup>2+</sup>, and agrees well with previous reports.<sup>47</sup> Due to the close binding energy values for the Zn 2p<sub>3/2</sub> reported in the literature for Zn<sup>2+</sup> in the form of ZnO or ZnFe<sub>2</sub>O<sub>4</sub> one cannot distinguish between the presence of ZnO or ferrite.<sup>45,51</sup> However, considering the surface enrichment observed in the XPS depth profile, together with the absence of a significant size reduction compared to undoped ferrite, we tentatively propose the formation of a Zn-rich ferrite shell with a graded concentration profile. This hypothesis is supported by the available data but would benefit from further confirmation by complementary structural techniques.

Additionally, post-reaction surface analysis (*e.g.*, XPS after H<sub>2</sub>O<sub>2</sub> exposure) is proposed as a valuable approach for future studies to directly monitor redox changes and surface evolution during ROS generation.

### 3.4 Understanding the role of ROS in the catalytic degradation mechanism

Table 3 summarizes the main radical species identified by EPR for each ferrite composition, together with the maximum signal intensity estimated from the double integration of the spectra obtained at 5 min reaction time. These values provide a comparative estimate of the relative concentration of radical species generated under identical conditions. Overall, these findings emphasize the complexity of the radical formation processes and underscore the importance of meticulously controlling and understanding experimental conditions.

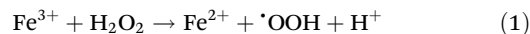
The choice of buffers and the method of particle oxidation are critical for accurately assessing the catalytic properties of nanomaterials. Moreover, the intrinsic nature of the samples

**Table 3** ROS generation of ferrite nanocatalysts

Sample	Main radical produced	Max. area (a.u.)
MW-Fe <sub>3</sub> O <sub>4</sub>	•OH	4.49
MW-γ-Fe <sub>2</sub> O <sub>3</sub>	•OOH	3.23
MW-γ-Fe <sub>2</sub> O <sub>3</sub> -8 nm	•OOH	7.94
MW-Mn <sub>0.4</sub> Fe <sub>2.6</sub> O <sub>4</sub>	•OOH	9.92
MW-Zn <sub>0.7</sub> Fe <sub>2.3</sub> O <sub>4</sub>	•OOH	0.66
MW-Co <sub>0.5</sub> Fe <sub>2.5</sub> O <sub>4</sub>	•OOH	3.98

plays a significant role; for instance, when working with non-oxidized iron oxide nanoparticles (magnetite), the predominant free radical produced is the •OH radical. In contrast, for maghemite samples or manganese doped-samples, the main radical generated is •OOH. Therefore, it is possible to design samples with specific characteristics depending on the application.

Understanding the role of transition metal cations in ROS generation requires examining their redox behavior within the spinel lattice to elucidate the underlying formation mechanisms. Given that Zn<sup>2+</sup> appears to suppress catalytic activity by passivating active sites, and that Co<sup>2+</sup> does not induce substantial changes in ROS generation under our experimental conditions, our mechanistic analysis is focused primarily on Mn-doped ferrites. In this sense, XPS analysis of MW-Mn<sub>0.4</sub>Fe<sub>2.6</sub>O<sub>4</sub> reveals that iron is predominantly present in the Fe<sup>3+</sup> oxidation state on the nanoparticle surface, with no significant evidence of surface Fe<sup>2+</sup>. This observation is expected given the known instability and ease of oxidation of Fe<sup>2+</sup> under ambient conditions. As a result, classical Fenton-type reactions involving Fe<sup>2+</sup> and H<sub>2</sub>O<sub>2</sub> to produce •OH are unlikely to occur efficiently under our conditions. Instead, Fe<sup>3+</sup> may participate in the reduction of H<sub>2</sub>O<sub>2</sub>, generating hydroperoxyl radicals •OOH through the following pathway:<sup>4</sup>



In contrast, *via* XPS analysis we confirmed that manganese is predominantly present in the Mn<sup>2+</sup> oxidation state with some Mn<sup>3+</sup> contribution. Although Mn<sup>2+</sup> is known to engage in Fenton-like reactions with H<sub>2</sub>O<sub>2</sub> to produce •OH, in our experiments, we observed limited reactivity reflected in the absence of •OH signatures in the EPR spectra of Mn-containing samples, suggesting that this pathway is not the dominant mechanism for ROS formation under our conditions.

Instead, we propose that the reaction using MW-Mn<sub>0.4</sub>Fe<sub>2.6</sub>O<sub>4</sub> proceeds *via* a redox cycle involving Mn<sup>3+</sup>/Mn<sup>2+</sup> transitions, with a strong catalase-like behavior. In this mechanism, Mn<sup>2+</sup> is first oxidized by H<sub>2</sub>O<sub>2</sub> to generate Mn<sup>3+</sup>, with the associated formation of hydroxide ions:



Mn<sup>3+</sup> can then react with a second molecule of hydrogen peroxide to regenerate Mn<sup>2+</sup> and yield molecular oxygen:





for sustainable chemical processes. In particular, designing efficient iron oxide ferrites for Fenton-based pollutant degradation in water can significantly reduce treatment costs at the industrial scale. Beyond environmental remediation, the ability to consistently produce clean water opens pathways for its reuse—either as potable water in regions where regulations allow or as input for other green technologies such as hydrogen production, which requires large volumes of purified water.

## Conflicts of interest

The authors declare that they have no known competing financial interests or personal relationships that could have appeared to influence the work reported in this paper.

## Data availability

The data supporting the findings of this study are included in the article and its ESI.† Additional raw data (e.g., TEM images, FTIR and EPR spectra, and numerical values used in the figures) are available from the corresponding author upon reasonable request.

## Acknowledgements

This work has received funding from the European Union's Horizon 2020 research and innovation programme under the Marie Skłodowska-Curie grant agreement No. 101007629 (NESTOR Project), the "Plan de Recuperación, Transformación y Resiliencia" financed by the European Union – NextGenerationEU under the Humidity-Plus project and from the Spanish Government (PID2023-1501700B-I00, TED2021-130191B-C43) by MCIU/AEI/ 10.13039/501100011033 and European Union NextGenerationEU/PRTR. FJP acknowledges financial support from Grants TED2021-132482B-I00 and PID2021-126169OB-I00 funded by MCIN/AEI/10.13039/501100011033 and by "ERDF A way of making Europe". The Servicio Interdepartamental de Investigación at the Universidad Autónoma de Madrid, the TEM Service at the Centro de Biología Molecular Severo Ochoa (CBMSO, CSIC-UAM), and XRD, FTIR and elemental analysis services at ICMM/CSIC are acknowledged for assistance for the characterization studies.

## References

- 1 M. Kurian, *Clean. Eng. Technol.*, 2021, **2**, 100090.
- 2 Z. Gao, J. Zhu, Q. Zhu, C. Wang and Y. Cao, *Sci. Total Environ.*, 2022, **847**, 157405.
- 3 I. M. F. Cardoso, R. M. F. Cardoso and J. C. G. Esteves da Silva, *Nanomaterials*, 2021, **11**(8), 2045.
- 4 N. Thomas, D. D. Dionysiou and S. C. Pillai, *J. Hazard. Mater.*, 2021, **404**, 124082.
- 5 S. Rahim Pouran, A. A. Abdul Raman and W. M. A. Wan Daud, *J. Clean. Prod.*, 2014, **64**, 24–35.
- 6 J. Wang and S. Wang, *Chem. Eng. J.*, 2020, **401**, 126158.
- 7 M. J. Davies, *Methods*, 2016, **109**, 21–30.
- 8 G. R. Eaton, S. S. Eaton, D. P. Barr and R. T. Weber, *Quantitative EPR*, Springer-Verlag, Germany, 2010.
- 9 A. Soufi, H. Hajjaoui, R. Elmoubarki, M. Abdennouri, S. Qourzal and N. Barka, *Appl. Surf. Sci. Adv.*, 2021, **6**, 100145.
- 10 R. Sharma and S. Singhal, *Clean – Soil, Air, Water.*, 2017, **46**(1), 1700605.
- 11 A. C. M. Maldonado, E. L. Winkler, M. Raineri, A. T. Córdova, L. M. Rodríguez, H. E. Troiani, M. L. M. Piscioti, M. V. Mansilla, D. Tobia, M. S. Nadal, T. E. Torres, E. De Biasi, C. A. Ramos, G. F. Goya, R. D. Zysler and E. Lima, *J. Phys. Chem. C*, 2019, **123**, 20617–20627.
- 12 L. Wang, J. Jiang, J. Ma, S. Pang and T. Zhang, *Chem. Eng. J.*, 2022, **427**, 131721.
- 13 S. Fernández-Velayos, F. J. Recio, F. J. Palomares, N. Menéndez, P. Herrasti and E. Mazarío, *J. Water Process Eng.*, 2023, **52**, 103549.
- 14 Y. Cheng, S. Zhang, Z. Wang, B. Wang, J. You, R. Guo and H. Zhang, *Sep. Purif. Technol.*, 2023, **318**, 123971.
- 15 S. Chakraborty, D. Menon, V. S. Akhil Varri, M. Sahoo, R. Ranganathan, P. Zhang and S. K. Misra, *Environ. Sci. Nano*, 2023, **10**, 1553–1569.
- 16 A. Gallo-Cordova, S. Veintemillas-Verdaguer, P. Tartaj, E. Mazarío, M. P. Morales and J. G. Ovejero, *Nanomaterials*, 2021, **11**(4), 1052.
- 17 C. Díaz-Ufano, A. Gallo-cordova, L. Santiandreu, S. Veintemillas-Verdaguer, R. Sáez-Puche, M. J. Torralvo-Fernandez and M. P. Morales, *Colloids Surf. A: Physicochem. Eng. Aspects*, 2023, **658**, 130695.
- 18 A. Gallo-Cordova, J. J. Castro, E. L. Winkler, E. Lima, R. D. Zysler, M. P. Morales, J. G. Ovejero and D. A. Streitwieser, *J. Clean. Prod.*, 2021, **308**, 127385.
- 19 A. Gallo-Cordova, B. Corrales-Pérez, P. Cabrero, C. Force, S. Veintemillas-Verdaguer, J. G. Ovejero and M. P. Morales, *Chem. Eng. J.*, 2024, **490**, 1–11.
- 20 N. Nuñez, E. Lima, M. Vásquez Mansilla, G. F. Goya, Á. Gallo-Cordova, M. P. Morales and E. L. Winkler, *Appl. Surf. Sci.*, 2024, **656**, 159655.
- 21 Á. Gallo-Cordova, A. Espinosa, A. Serrano, L. Gutiérrez, N. Menéndez, M. P. Morales and E. Mazarío, *Mater. Chem. Front.*, 2020, **4**, 3063–3073.
- 22 A. Gallo-Cordova, J. G. Ovejero, A. M. Pablo-Sainz-Ezquerria, J. Cuya, B. Jeyadevan, S. Veintemillas-Verdaguer, P. Tartaj and M. P. Morales, *J. Colloid Interface Sci.*, 2022, **608**, 1585–1597.
- 23 F. L. Rivera, F. J. Recio, F. J. Palomares, J. Sánchez-Marcos, N. Menéndez, E. Mazarío and P. Herrasti, *J. Electroanal. Chem.*, 2020, 114773.
- 24 S. Ammar and F. Fiévet, *Nanomaterials*, 2020, **10**, 1–8.
- 25 K. I. Hadjiivanov, D. A. Panayotov, M. Y. Mihaylov, E. Z. Ivanova, K. K. Chakarova, S. M. Andonova and N. L. Drenchev, *Chem. Rev.*, 2021, **121**, 1286–1424.



- 26 Á. Delgado, Á. Gallo-Córdova, C. Díaz-Ufano, E. Martín, V. Blanco-Gutiérrez, M. P. Morales, M. J. Torralvo and R. Sáez, *J. Phys. Chem. C*, 2023, **127**, 4714–4723.
- 27 K. Simeonidis, M. P. Morales, T. Damartzis, N. Maniotis and S. Veintemillas-Verdaguer, *Ind. Eng. Chem. Res.*, 2024, **63**, 20651–20660.
- 28 R. Herscu-Kluska, A. Masarwa, M. Saphier, H. Cohen and D. Meyerstein, *Chem. – Eur. J.*, 2008, **14**, 5880–5889.
- 29 A. Millan, A. Urtizberea, N. J. O. Silva, F. Palacio, V. S. Amaral, E. Snoeck and V. Serin, *J. Magn. Magn. Mater.*, 2007, **312**, L5–L9.
- 30 M. Raineri, E. L. Winkler, T. E. Torres, M. Vasquez Mansilla, M. S. Nadal, R. D. Zysler and E. Lima, *Nanoscale*, 2019, **11**, 18393–18406.
- 31 P. J. Lin, C. H. Yeh and J. C. Jiang, *RSC Adv.*, 2021, **11**, 36257–36264.
- 32 P. Kumar, V. Tomar, D. Kumar, R. K. Joshi and M. Nemiwal, *Tetrahedron*, 2022, **106–107**, 132641.
- 33 H. Ghorbani, M. Eshraghi and A. A. Sabouri Dodaran, *Physica B: Condens. Matter*, 2022, **634**, 413816.
- 34 M. Bhuvanawari, S. Sendhilmathan, M. Kumar, R. Tamilarasan and N. V. Giridharan, *Mater. Sci. Polym.*, 2016, **34**, 344–353.
- 35 C. Rath, S. Anand, R. P. Das, K. K. Sahu, S. D. Kulkarni, S. K. Date and N. C. Mishra, *J. Appl. Phys.*, 2002, **91**, 2211–2215.
- 36 A. C. Moreno Maldonado, E. L. Winkler, M. Raineri, A. T. Córdova, L. M. Rodríguez, H. E. Troiani, M. L. M. Piscioti, M. V. Mansilla, D. Tobia, M. S. Nadal, T. E. Torres, E. De Biasi, C. A. Ramos, G. F. Goya, R. D. Zysler and E. Lima, *J. Phys. Chem. C*, 2019, **123**, 20617–20627.
- 37 Y. Li, J. He, K. Zhang, P. Hong, C. Wang, L. Kong and J. Liu, *J. Mater. Sci.*, 2020, **55**, 13767–13784.
- 38 V. E. Oldham, M. R. Jones, B. M. Tebo and G. W. Luther, *Mar. Chem.*, 2017, **195**, 122–128.
- 39 S. Zhang, J. Lv, R. Han, Z. Wang, P. Christie and S. Zhang, *Water Res.*, 2021, **196**, 117034.
- 40 W. H. Koppenol and R. H. Hider, *Free Radicals Biol. Med.*, 2019, **133**, 3–10.
- 41 M. Gu, D. C. Bode and J. H. Viles, *Sci. Rep.*, 2018, **8**, 1–14.
- 42 C. Hübner and H. Haase, *Redox Biol.*, 2021, **41**, 101916.
- 43 K. A. McCall, C. C. Huang and C. A. Fierke, *J. Nutr.*, 2000, **130**, 1437S–1446S.
- 44 M. K. Lima-Tenório, L. A. S. Oliveira, M. R. Guilherme, E. T. Tenório-Neto, M. F. Silva, D. M. Fernandes, A. A. W. Hechenleitner and E. A. G. Pineda, *Mater. Lett.*, 2017, **195**, 151–155.
- 45 M. C. Biesinger, B. P. Payne, A. P. Grosvenor, L. W. M. Lau, A. R. Gerson and R. S. C. Smart, *Appl. Surf. Sci.*, 2011, **257**, 2717–2730.
- 46 J. Rubio-Zuazo, A. Chainani, M. Taguchi, D. Malterre, A. Serrano and G. R. Castro, *Phys. Rev. B*, 2018, **97**, 1–9.
- 47 C. Pascual-González, H. Amorín, R. P. del Real, F. Serrano-Sánchez, F. J. Palomares, A. Castro and M. Algueró, *Ceram. Int.*, 2024, **50**, 53562–53570.
- 48 E. S. Ilton, J. E. Post, P. J. Heaney, F. T. Ling and S. N. Kerisit, *Appl. Surf. Sci.*, 2016, **366**, 475–485.
- 49 A. J. Nelson, J. G. Reynolds and J. W. Roos, *J. Vac. Sci. Technol., A*, 2000, **18**, 1072–1076.
- 50 T. Scientific, Manganese X-ray photoelectron spectra, manganese electron configuration, and other elemental information.
- 51 A. Y. Lee, *NIST X-ray Photoelectron Spectroscopy Database*, 2023, DOI: [10.18434/T4T88K](https://doi.org/10.18434/T4T88K).
- 52 N. Singh, M. Geethika, S. M. Eswarappa and G. Mugesh, *Chem. – Eur. J.*, 2018, **24**, 8393–8403.
- 53 Y. Li, J. Sun and S. P. Sun, *J. Hazard. Mater.*, 2016, **313**, 193–200.
- 54 Y. Wen, J. Yan, B. Yang, Z. Zhuang and Y. Yu, *J. Mater. Chem. A*, 2022, **10**, 19184–19210.
- 55 F. S. Archibald and I. Fridovich, *Arch. Biochem. Biophys.*, 1982, **214**, 452–463.
- 56 R. J. Watts, J. Sarasa, F. J. Loge and A. L. Teel, *J. Environ. Eng.*, 2005, **131**, 158–164.

